Multiphase Thermohaline Convection in the Earth's Crust: II. Benchmarking and Application of a Finite Element – Finite Volume Solution Technique with a NaCl–H₂O Equation of State

SEBASTIAN GEIGER[1,*], THOMAS DRIESNER[1],
CHRISTOPH A. HEINRICH[1] and STEPHAN K. MATTHÄI[2]

[1]*Department of Earth Sciences, Institute for Isotope Geology and Mineral Resources, ETH Zürich, Sonneggstr. 5, CH-8092 Zürich, Switzerland*
[2]*Department of Earth Science and Engineering, Imperial College London, SW7 2AZ, U.K.*

Abstract. We present the benchmarking of a new finite element – finite volume (FEFV) solution technique capable of modeling transient multiphase thermohaline convection for geological realistic $p-T-X$ conditions. The algorithm embeds a new and accurate equation of state for the NaCl–H₂O system. Benchmarks are carried out to compare the numerical results for the various component-processes of multiphase thermohaline convection. They include simulations of (i) convection driven by temperature and/or concentration gradients in a single-phase fluid (i.e., the Elder problem, thermal convection at different Rayleigh numbers, and a free thermohaline convection example), (ii) multiphase flow (i.e., the Buckley–Leverett problem), and (iii) energy transport in a pure H₂O fluid at liquid, vapor, supercritical, and two-phase conditions (i.e., comparison to the U.S. Geological Survey Code HYDROTHERM). The results produced with the new FEFV technique are in good agreement with the reference solutions. We further present the application of the FEFV technique to the simulation of thermohaline convection of a 400°C hot and 10 wt.% saline fluid rising from 4 km depth. During the buoyant rise, the fluid boils and separates into a high-density, high-salinity liquid phase and a low-density, low-salinity vapor phase.

Key words: brine, vapor, hydrothermal, porphyry copper, mid-ocean ridge, two-phase flow, convection, numerical modeling, finite element, finite volume, NaCl–H₂O, benchmarking.

Nomenclature

a Dispersion coefficient [m].
$\mathcal{C}$ Courant criterion [s].
c_p Isobaric heat capacity [kJ kg^{-1} °C^{-1}].
D Diffusivity [m² s^{-1}].

*Author for correspondence: e-mail: geiger@erdw.ethz.ch

$\mathbf{g}$ Gravitational acceleration vector [$\mathrm{m\,s^{-2}}$].
k_r Relative permeability [–].
$\mathbf{k}$ Permeability tensor [$\mathrm{m^2}$].
K Thermal conductivity [$\mathrm{W\,m^{-1}\,{}^\circ C^{-1}}$].
Nu Nusselt number [–].
p Pressure [Pa] or [bar].
Pe Peclet number [–].
Ra Rayleigh number [–].
S Saturation [–].
t Time [s].
T Temperature [$^\circ$C].
$\mathbf{v}$ Velocity [$\mathrm{m\,s^{-1}}$].
x Mass fraction fluid [–].
X Salinity [wt.% NaCl].

Greek Symbols

α Thermal expansivity [$^\circ\mathrm{C}^{-1}$].
β Compressibility [Pa^{-1}].
γ Chemical expansivity [$\mathrm{wt.\%\ NaCl}^{-1}$].
δ General diffusivity parameters [$\mathrm{m^2\,s^{-1}}$].
Δ Increment [–].
μ Viscosity [Pa s].
κ Thermal diffusivity [$\mathrm{m^2\,s^{-1}}$].
ϕ Porosity [–].
ψ General conserved variable [e.g., $\mathrm{kg\,m^{-3}}$].
ρ Density [$\mathrm{kg\,m^{-3}}$].
σ Heat capacity ratio [–].

Subscripts and Superscripts

f Fluid (all fluid phases present).
i Fluid phase.
l Liquid phase.
L Longitudinal.
p Pore space.
r Rock phase.
T Transversal.
th   Thermal.
v Vapor phase.

1. Introduction

The setting of many geologic processes, such as deep fluid convection in magmatic hydrothermal systems, commonly precludes direct observation of active fluid flow. Hence, indirect observations such as fluid inclusions measurements and chemical data are used to decipher potential flow scenarios (Roedder, 1971; Nehlig *et al.*, 1991; von Damm, 1995; Heinrich *et al.*, 1999) and often indicate that fluid flow involves the simultaneous convection of heat and salt. The data, however, commonly yield only an incom-

plete or time-integrated picture. Numerical simulations of such thermohaline convective systems hence would provide a valuable tool to analyze the temporal and spatial evolution of hydrothermal fluid flow.

Numerical simulations of flow in magmatic hydrothermal systems have so far been seriously hampered for two reasons. On the one hand, although the properties of pure H_2O are well known (Haar et al., 1984), the lack of an equation of state for the NaCl–H_2O system that is valid over the large temperature, pressure, and compositional range that can be encountered in magmatic hydrothermal systems is missing. On the other hand, computational tools capable of modelling energy transport (Pruess, 1987, 1991; Hayba and Ingebritsen, 1994; Zyvoloski et al., 1996) usually lack the ability to model salt transport in two fluid phases and are sometimes restricted to staggered grids that cannot resolve complex geologic structures accurately. Hence, studies of thermohaline convection in magmatic hydrothermal systems have mostly been limited to incompressible single-phase flow of thermohaline convection including linear $T - X$ approximations for the fluid density ρ and constant viscosities (Schoofs, 1999), or to energy transport in a pure water fluid (Cathles, 1977; Norton and Knight, 1977; Delaney 1982; Dutrow and Norton, 1995; Hayba and Ingebritsen, 1997; Jupp and Schultz, 2000). While these studies have revealed fundamental insight into the time scales and flow patterns in hydrothermal systems, their results do not account for the fact that NaCl–H_2O fluids can separate into a high-density, high-salinity liquid phase and low-density, low-salinity vapor phase at temperatures and pressures well above the critical temperature and pressure of pure H_2O (Sourirajan and Kennedy, 1962). Studies of heat transport in pure H_2O further cannot account for the fact that thermohaline convection exhibits a complex double-diffusive, double-convective behavior (Phillips, 1991; Schoofs, 1999).

To overcome the limitations and simplifying assumptions of previous studies of fluid flow in magmatic hydrothermal systems, we use the older version (Driesner and Heinrich, 2003) of a new equation of state for the NaCl–H_2O system valid from 0 to 750°C, 0 to 4000 bar, and 0 to 100 wt.% NaCl (Driesner, 2005; Driesner and Heinrich, 2005). The equation is utilized by our novel finite element – finite volume (FEFV) algorithm. Our solution technique is capable of modeling the simultaneous transport of heat and salt in two fluid phases with highly varying fluid properties (Geiger et al., 2005). This FEFV formulation permits a flexible discretization of complex geological structures (Geiger et al., 2004). The development of the governing equations, numerical methods, and thermodynamic fluid properties are discussed in an accompanying paper (Geiger et al., 2006).

Unfortunately, no physical experiments of multiphase thermohaline convection in porous media or comparable codes exist which can be used to benchmark and verify our new solution technique. The different

sub-processes of multiphase thermohaline convection, however, are intensely studied and well understood. These processes comprise multiphase flow, solute transport, single-phase convection driven by temperature and/or salinity gradients, and energy transport with phase transitions. It is hence possible to conduct a series of benchmark tests for these component processes.

The benchmarking presented in this paper demonstrates the ability of our FEFV algorithm to properly calculate the convection of heat and salt during the simultaneous flow of a high-density, high-salinity liquid phase and a low-density, low-salinity vapor phase. In particular, we verify that (i) the operator splitting technique employed in our algorithm accurately models the advection and diffusion of a solute (Strang, 1968), (ii) the simultaneous flow of two incompressible fluids yields accurate results when compared to the analytical solution of the Buckley–Leverett problem (Buckley and Leverett, 1942; Helmig, 1997), (iii) convection of salt yields the correct results when compared to the classical Elder problem (Elder, 1967), (iv) convection of heat in an incompressible pure H_2O fluid can be properly resolved at various Rayleigh numbers (Caltagirone, 1975), (v) convection of heat and salt in a single, slightly compressible fluid yields the correct behavior for the separation of the thermal and salt plumes for different initial buoyancy configurations (Oldenburg and Pruess, 1999), and (vi) that energy transport in a pure H_2O fluid can be accurately modeled at liquid, vapor, and supercritical conditions and for the case where a vapor phase displaces a liquid phase. This is achieved by comparing our numerical results to the well-established U.S. Geological Survey Code HYDRO-THERM (Hayba and Ingebritsen, 1994).

Finally, we show an application of multiphase thermohaline convection where a hot, saline and initially single-phase fluid rises and starts to boil. Upon phase separation, the high-density, high-salinity liquid phase sinks down and the low-density, low salinity vapor phase rises quickly.

2. Governing Equations and Numerical Solution

The derivation of the governing equations and the development of the numerical solution algorithm are discussed in detail in the companion paper (Geiger *et al.*, 2005). Formulated in terms of fluid pressure p, temperature T, and salinity X, conservation for energy is given by

$$
\begin{aligned}
\big((1-\phi)\,\rho_r c_{pr} &+ \phi\left(S_l \rho_l c_{pl} + S_v \rho_v c_{pv}\right)\big)\frac{\partial T}{\partial t} \\
&= -\nabla \cdot \left(\mathbf{v}_v c_{pv}\rho_v T\right) - \nabla \cdot \left(\mathbf{v}_l c_{pl}\rho_l T\right) + \nabla \cdot (K\nabla T)
\end{aligned}
\tag{1}
$$

conservation of salt by

$$\phi \frac{\partial}{\partial t} \rho_f X_f = -\nabla \cdot (\mathbf{v}_v \rho_v X_v) - \nabla \cdot (\mathbf{v}_l \rho_l X_l) +$$
$$+ \nabla \cdot (\mathbf{D}_l \nabla \rho_l X_l) + \nabla \cdot (\mathbf{D}_v \nabla \rho_v X_v) \qquad (2)$$

and for fluid mass written in terms of a fluid pressure evolution by

$$\rho_f \left(\beta_r + \phi \beta_f \right) \frac{\partial p}{\partial t} = \nabla \cdot \left[\mathbf{k} \left(\frac{k_{rl}}{\mu_l} \rho_l + \frac{k_{rv}}{\mu_v} \rho_v \right) \nabla p \right] +$$
$$+ \mathbf{k} \left(\frac{k_{rl}}{\mu_l} \rho_l^2 + \frac{k_{rv}}{\mu_v} \rho_v^2 \right) g \nabla z + \phi \rho_f \left(\gamma_f \frac{\partial X}{\partial t} - \alpha_f \frac{\partial T}{\partial t} \right). \qquad (3)$$

The velocity $\mathbf{v}$ at which phase i moves is given by

$$\mathbf{v}_i = -\mathbf{k} \frac{k_{ri}}{\mu_i} \left[\nabla p - \rho_i \mathbf{g} \right]. \qquad (4)$$

In the above equations, ρ is the fluid density, μ the fluid viscosity, S the phase saturation, c_p the isobaric heat capacity, K the thermal conductivity, $\mathbf{D}$ the dispersion tensor, $\mathbf{k}$ the permeability tensor, ϕ the porosity, β the compressibility, α the thermal expansivity, γ the chemical expansivity, k_r the relative permeability, and $\mathbf{g} = [0, 0, -g]^T$ the gravitational acceleration vector. The subscripts l, v, and r refer to the liquid, vapor, and rock phase, respectively. The subscript f refers to the total fluid mixture, i.e., $\rho_f = S_l \rho_l + S_v \rho_v$, $\rho_f X_f = S_l \rho_l X_l + S_v \rho_v X_v$, and $X_f = (S_l \rho_l X_l + S_v \rho_v X_v) / (S_l \rho_l + S_v \rho_v)$.

We solve the governing equations sequentially and decoupled, modelling parabolic (diffusion) equations with the finite element method and hyperbolic (advection) equations with the finite volume method. The key advantages of this FEFV formulation over a fully coupled formulation are that the global solution matrices are better conditioned and hence are suitable for fast (algebraic) multigrid solvers, that costly iterative schemes are omitted, that although the size of the time-step is restricted due to the CFL criterion, the runtime is favorably faster in the decoupled approach, and that the geometric flexibility of the finite element method is retained (Geiger et al., 2005). The new equation of state for NaCl–H$_2$O (Driesner and Heinrich, 2003, 2005; Driesner, 2005) provides the fluid properties ρ, c_p, μ, S, β, α, and γ as a function of p, T, and X.

3. Tests for Accuracy and Benchmarks for Speed

3.1. COMPARISON TO ANALYTICAL SOLUTIONS

The comparison of numerical and analytical solutions for linear, incompressible single-phase transport and non-linear, incompressible two-phase

flow was used to test the accuracy of the operator splitting and decoupling approaches inherent in our FEFV method.

3.1.1. *Advection Diffusion Equation*

We compare the numerical results and the analytical solution of the generic one-dimensional advection-diffusion equation in an incompressible fluid at various Péclet numbers, i.e. different ratios between solute transport due to advection and diffusion (Figure 1). The generic one-dimensional advection-diffusion equation is

$$\frac{\partial \psi}{\partial t} = -\mathbf{v}_x \frac{\partial}{\partial x} \psi + \delta \frac{\partial^2}{\partial x^2} \psi. \tag{5}$$

It has the well-known analytical solution (Ogata and Banks, 1961)

$$\psi(x, t) = \frac{\psi_{x=0}}{2} \text{erfc} \left[\frac{x - \mathbf{v}_x t}{2\sqrt{\delta t}} \right] + \frac{\psi_{x=0}}{2} \exp \left[\frac{\mathbf{v}_x x}{\delta} \right] \text{erfc} \left[\frac{x + \mathbf{v}_x t}{2\sqrt{\delta t}} \right], \tag{6}$$

where ψ is the conserved quantity, δ the diffusivity, and erfc the complementary error function. Excellent agreement between the numerical and
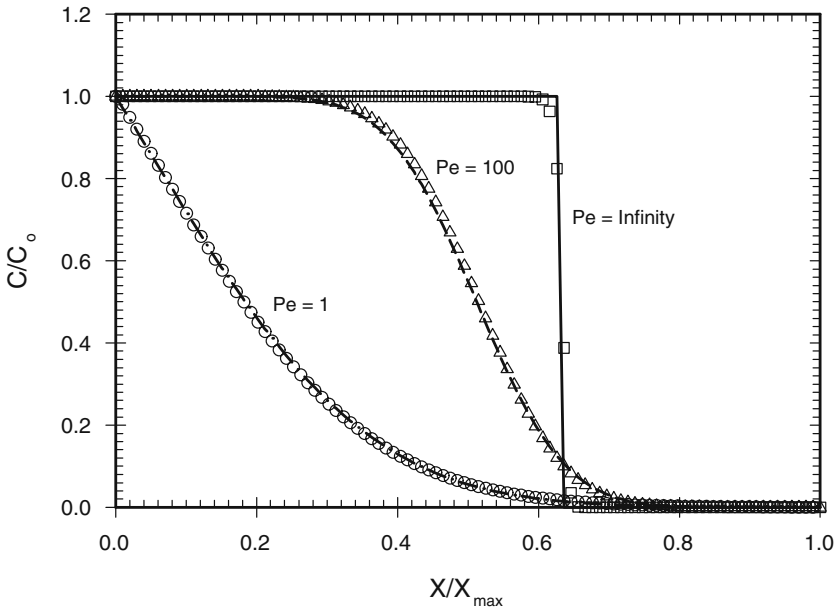

Figure 1. Comparison between numerical (open symbols) and analytical (lines) solutions for the generic advection-diffusion equation (Equation (5)) at different Péclet numbers for solute transport in an incompressible fluid. The normalized grid resolution $\Delta x/x_{\max}$ is $\Delta x/x_{\max} = 0.0101$. Transport includes pure advection at $Pe = \infty$ (squares and solid lines), diffusion dominated at $Pe = 100$ (circles and dashed-dotted lines), and an intermediate cases at $Pe = 1$ (triangles and dashed lines). The time-step Δt is given by the CFL criterion $\mathcal{C}$, i.e, $\Delta t = \mathcal{C}$.

analytical solutions, specifically for the purely advective case ($Pe = \infty$), is obtained (Figure 1). In the latter case, the jump in concentration is resolved within three nodes. The exact representation of this discontinuity is the result of the spatially second-order accurate finite volume scheme employed in the FEFV method (Geiger *et al.*, 2004).

3.1.2. *Buckley–Leverett Problem*

A classical test problem for the accuracy of a numerical method for incompressible two-phase flow is the Buckley–Leverett problem for which an analytical solution can be derived (Buckley and Leverett, 1942; Helmig, 1997).

In the Buckley–Leverett problem, a wetting phase w displaces a non-wetting phase n. The two phases are immiscible. A one-dimensional domain is initially entirely saturated with the non-wetting phase ($S_w = 0$). The wetting phase enters the domain at a saturation of $S_w = 1$, flows down a pressure gradient, and displaces the non-wetting phase. A discontinuity (shock front) originates where the wetting phase first displaces the non-wetting phase. Once the pores are largely filled with the wetting phase, the non-wetting phase becomes increasingly immobile. Left, i.e. upstream, of the shock front, the nonlinear relative permeability model causes a nonlinear variation (rarefaction fan) from the maximum wetting-phase saturation value at the shock front ($S_w \sim 0.78$) to the original wetting-phase saturation value at the inlet boundary ($S_w = 1.0$). This test hence also indicates how well a numerical method can deal with a non-linear flow problem.

We compare numerical solutions for the Buckley–Leverett problem with the analytical solution. Table I lists the fluid and rock properties. Assuming that the two fluids are incompressible, their viscosities are equal, and that gravitational and capillary effects are absent, the governing equations (Equations (1)–(3)) reduce to

$$0 = \nabla \cdot \left[\mathbf{k} \left(\frac{k_{rn}}{\mu_n} + \frac{k_{rw}}{\mu_w} \right) \nabla p \right],$$

$$\phi \frac{\partial S_i}{\partial t} = -\nabla \cdot \mathbf{v}_i \quad i \in \{n, w\}. \tag{7}$$

In our simulations, numerical and analytical solutions show excellent agreement (Figure 2). The rarefaction fan and shock front are accurately resolved and the solution converges as the grid is refined. The shock front is resolved within three nodes, independent of the grid size. Using the five-spot waterflood problem (Spivak *et al.*, 1977); Geiger *et al.* (2004) have shown that this method accurately solves for (two-phase) fluid flow in different directions relative to the grid orientation. The suitability of the numerical method to simulate two-phase flow on unstructured grids with highly heterogeneous permeability fields was also shown by Geiger *et al.* (2004).

Table I. Input parameters for all benchmark tests

Buckley–Leverett problem

ϕ	0.1	[-]
k	1.0×10^{-14}	[m^2]
dp/dx	1.0×10^3	[Pa m^{-1}]
$\mu_w = \mu_n$	0.0001	[Pa s]
k_{rw}	S_w^4	[-]
k_{rn}	$(1 - S_w)^2 (1 - S_w^2)$	[-]

Elder problem

ϕ	0.1	[-]
k	4.845×10^{-13}	[m^2]
$\mathbf{D}_l = D_l$	3.565×10^{-6}	[m^2 s^{-1}]
μ_l	0.001	[Pa s]
$\rho_{l,t=0}$	1000	[kg m^{-3}]
ρ_l	$1000 + 200 \times X_l$	[kg m^{-3}]

Free thermal convection

ρ_l	$\rho_{z=0} (1 - \alpha (T - T_{z=0}))$	[kg m^{-3}]
$\mu_l, \kappa, \mathbf{k}, \alpha$	Function of Ra_{th}	

Free thermohaline convection

ϕ	0.1	[-]
k	5.0×10^{-14}	[m^2]
ρ_r	2650	[kg m^{-3}]
c_{pr}	1.0	[kJ kg^{-1} °C^{-1}]
K	1.8	[W m^{-1} °C^{-1}]
D_p	1.0×10^{-8}	[m^2 s^{-1}]
$T_{t=0}$	200.0	[°C]
$X_{t=0}$	0.0	[wt.% NaCl]
$\rho_{l,t=0}$	875.0	[kg m^{-3}]

Energy benchmark

ϕ	0.1	[-]
ρ_r	2750	[kg m^{-3}]
c_{pr}	0.88	[kJ kg^{-1} °C^{-1}]
K	2.25	[W m^{-1} °C^{-1}]

3.2. CONVECTION BENCHMARKS

We have verified the suitability of our numerical method to model free convection driven by concentration and/or temperature gradients by comparing the obtained results with published results for a series of classical benchmarks tests for single-phase flow.
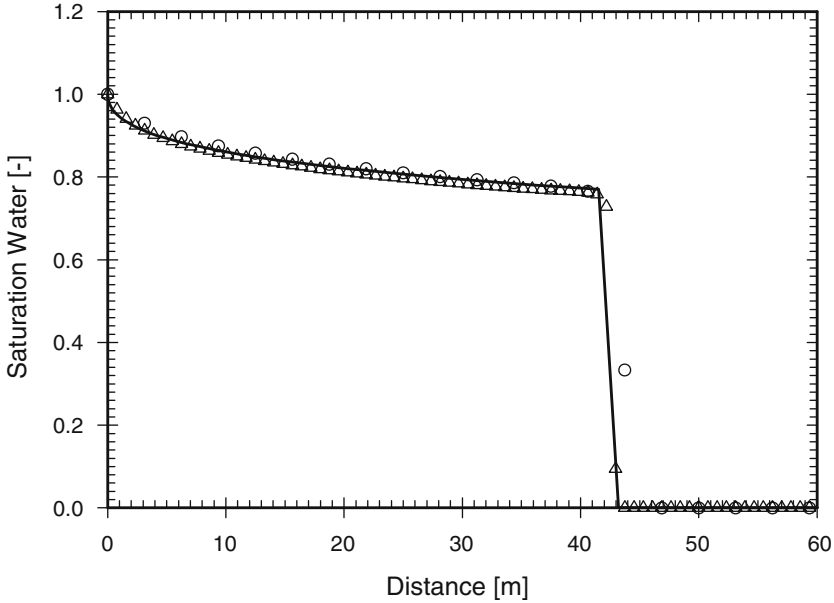
Figure 2. Comparison of the one-dimensional numerical solution (open symbols) for a coarse (circles) and fine (triangles) grid to the analytical (solid line) solution of the Buckley–Leverett problem. The wetting phase w displaces the non-wetting phase n in a homogeneous porous medium.

3.2.1. *Elder Problem*

The classical benchmark test to validate a code for modeling free convection driven by concentration gradients is the Elder problem (Elder, 1967). In the Elder problem, a saline fluid that is 20% denser than pure water sinks downwards from the top boundary, driven by buoyancy forces only. The domain is a rectangular box of $600 \times 150\,\text{m}$ of saturated, homogeneous, and isotropic porous medium (Figure 3). The Elder problem is very suitable for testing density-dependent fluid flow because the flow pattern is entirely determined by the internal balance of the gravitational and pressure forces (Simpson and Clement, 2003). For this test-case, the governing equations (Equations (1–3)) reduce to

$$\phi \frac{\partial}{\partial t} \rho_l X_l = -\nabla \cdot (\mathbf{v}_l \rho_l X_l) + \nabla \cdot (\mathbf{D}_l \nabla \rho_l X_l),$$

$$\rho_l \phi \beta_f \frac{\partial p}{\partial t} = \nabla \cdot \left[\mathbf{k} \left(\frac{1}{\mu_l} \rho_l \right) \nabla p \right] + \mathbf{k} \left(\frac{1}{\mu_l} \rho_l^2 \right) g \nabla z + \phi \rho_l \gamma \frac{\partial X_l}{\partial t}. \tag{8}$$

The parameters for the classical configuration are listed in Table I. The obtained results are in very good agreement with results published for similarly fine meshes in Koldtiz *et al.* (1998) and Ackerer *et al.* (1999) (Figure 3). The flow patterns are axisymmetric with a central up-flow zone
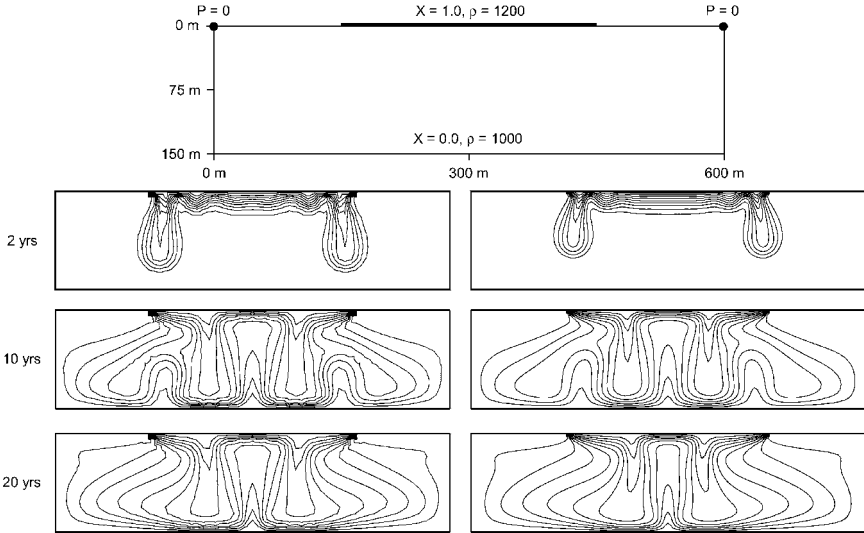
Figure 3. Solution to the Elder problem showing the salt concentrations for a coarse grid (left) and fine grid (right) consisting of 2048 and 8192 uniform triangular finite elements, respectively, at 2, 10, and 20 years (top to bottom). Contour lines show the salinity in 0.1 intervals from 0.0 to 1.0 wt.% NaCl.

bordered by two down-flow zones. Our solutions to the Elder problem are less sensitive to grid resolution than the reference solutions (Kolditz *et al.*, 1998; Ackerer *et al.*, 1999). This becomes evident in the salt concentrations, which do not change significantly with a mesh refinement by a factor four. This suggests mesh convergence is obtained already on the coarse mesh. The second order accurate advection scheme contributes to the fast mesh convergence. The runtime properties are shown in Figure 4. The runtime increases with the power of ∼1.5 with increasing mesh refinement.

3.2.2. *Thermal Convection*

Free thermal convection at high Raleigh numbers in a closed square domain has been extensively studied (Caltagirone, 1975; Kimura *et al.*, 1986; Steen and Aidun, 1988; Caltagirone and Fabrie, 1989; Cherkaoui and Wilcock, 1999; Schoofs, 1999) and serves as a test-case for the ability of our numerical method to resolve small scale features. In this test-case, a constant basal temperature is applied. The temperature at the top boundary is held constant as well. Normally, the Boussinesq approximation is employed in those simulations, i.e., the assumptions that the fluid is a single-phase incompressible liquid ($\beta = 0$) and that the density term can be neglected everywhere ($\alpha = \gamma = 0$) but in the buoyancy term $\rho\mathbf{g}$ in the fluid pressure equation (Equation (3)). As a result, the divergence of the fluid velocity is zero, i.e., $\nabla \cdot \mathbf{v}_l = 0$. The governing equations (Equations (1)–(3)) reduce to (Caltagirone, 1975).
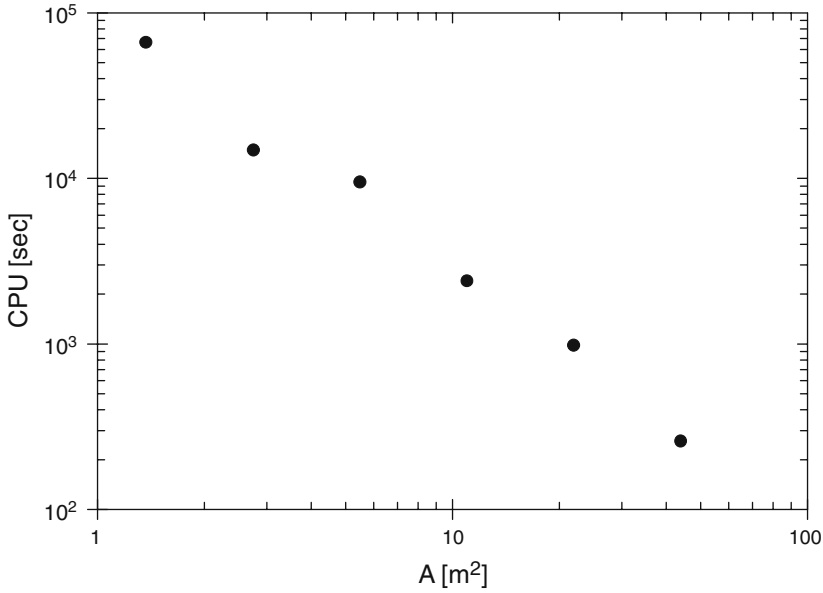
Figure 4. CPU time for the Elder Problem plotted as a function of the area of an individual finite element. Simulations where carried out with a Intel P4 (2.2 GHz) processor. The coarsest mesh comprises 2048 finite elements, the finest mesh 65536 elements.

$$\sigma \frac{\partial T}{\partial t} = -\nabla \cdot (\mathbf{v}_l T) + \nabla \cdot (\kappa \nabla T),$$
$$0 = \nabla \cdot \left[\mathbf{k} \left(\frac{1}{\mu_l} \right) \nabla p \right] + \mathbf{k} \left(\frac{1}{\mu_l} \rho_l \right) g \nabla z, \qquad (9)$$

where σ is the ratio of the volumetric heat capacities in rock and fluid $\sigma = (c_{pr} \rho_r) / (c_{pl} \rho_l)$. It is commonly assumed that $\sigma \approx 1$. κ is the thermal diffusivity $\kappa = K / (c_{pl} \rho_l)$. In the simulations, the thermal Rayleigh number Ra_{th}

$$Ra_{\text{th}} = \frac{(\rho_{\max} - \rho_{z=0}) \, g z \mathbf{k}_z}{\mu_l \kappa} \qquad (10)$$

is computed for fixed values of $\mu_l, \kappa, \mathbf{k}, x_{\max} = z_{\max}, T_{z=0}, T_{\max}, \rho_{z=0}$, and α. The density is computed as a linear function of T (Table I). The dimensionless heat transport, expressed as the horizontally averaged thermal Nusselt number Nu_{th}

$$Nu_{\text{th}} = -\frac{\partial \overline{T}}{\partial \overline{z}} \qquad (11)$$

is measured at the top of the domain as a function of Ra_{th}. In the definition of Nu_{th}, the bar denotes the normalized quantity $\overline{z} = z / z_{\max}$ and $\overline{T} = (T - T_{z=0}) / (T_{\max} - T_{z=0})$. The results of Nu_{th} obtained for a given

Table II. Comparison of the average thermal Nusselt number Nu_{th} for closed-top convection in a square domain

Ra_{th}	Nu_{th}						
	This study	1	2	3	4	5	6
100	2.560	2.65	–	2.651	–	2.647	2.643
200	3.818	3.81	–	3.810	–	3.801	3.806
300	4.503	4.52	–	4.523	–	4.519	4.511
500*	5.87	–	5.90	–	5.86	5.82	5.86
800*	9.62	–	9.30	–	9.42	9.14	9.07

The star denotes unsteady convection. Column entries are 1 = Caltagirone (1975), 2 = Kimura *et al.* (1986), 3 = Steen and Aidun (1988), 4 = Caltagirone and Fabrie (1989), 5 = Cherkaoui and Wilcock (1999), 6 = Schoofs (1999).

Figure 5. Oscillatory convection at Ra_{th} 800. The evolution of the normalized temperature $\overline{T}$ is shown at three different time-steps for one oscillatory cycle. Small convection cells shear off at the bottom boundary at a characteristic dimensionless frequency of 270 and merge with the main plume in the center. At $Ra = 800$, other studies reported dimensionless frequencies of 280 (Kimura *et al.*, 1986), 296 (Caltagirone and Fabrie, 1989), 299.7 (Cherkaoui and Wilcock, 1999), and 287.2 (Schoofs, 1999). Contour levels are in 0.1 intervals from 0.0 to 1.0.

Ra_{th} (Table II) are in good agreement with the published results and small differences can be explained by the different choices of discretization. Figure 5 shows the evolution of the normalized temperature field over one oscillatory cycle at $Ra_{th} = 800$. Here, the measured frequency is the lowest of all other published frequencies but is still in relatively good agreement with the other data.

3.2.3. *Thermohaline Convection*

The separation of the thermal plume and the salt plume by transient thermohaline double-advective convection for a NaCl–CaCl$_2$–H$_2$O brine has recently been studied numerically (Oldenburg and Pruess, 1999). Here, the full set of governing equations (Equations (1–3)) can be applied with $S_l = 1$

and $S_v = 0$, i.e., no vapor phase present. Our simulations use a different equation of state, but the differences between our NaCl–H$_2$O model and the NaCl–CaCl$_2$–H$_2$O equation of state in Oldenburg and Pruess, (1999) are small. However, because Oldenburg and Pruess, (1999) assume that the concentration of CaCl$_2$ is low we have adjusted our initial NaCl concentration to obtain similar fluid densities (Table III).

This benchmark is very useful for two reasons. First, the simulations do not rely on the Boussinesq approximation. Instead the fluids are treated correctly as slightly compressible. Second, the qualitative behavior of plume separation can be verified. The input properties for the initial parcel are listed in Tables I and III. The initial and boundary conditions are shown in Figure 6. The initial rock and fluid properties for both simulations are listed in Table I. We discretized the domain using 8192 triangular finite elements (4425 finite volumes), which results in a uniform nodal spacing of 39.06 m. The grid spacing is 100.0 m in Oldenburg and Pruess (1999).

The results of the numerical solutions show the correct behavior and, although the employed equation of states describe different fluid compositions, the spatial and temporal evolution of the fronts agree very well. When the hot brine parcel is buoyant, the overall motion of fluid is upward. Because the temperature front is thermally retarded, a high-density lid develops on top of a low-density region. This retards the overall movement of the plume but the motion of the thermal and salt plume is still upward (Figure 7). When the hot brine parcel is negatively buoyant, the thermal and brine plumes separate. The high-density zone that evolves below the initial parcel location accelerates the downward-motion of brine while the thermal plume rises after plume separation (Figure 8).

Table III. Input parameters for the free thermohaline convection problem as used in this study and by Oldenburg and Pruess (1999)

Property	This study	Oldenburg and Pruess (1999)	Unit
T_+	300.0	300.0	[°C]
X_+	10.0	11.6	[wt.% NaCl]
ρ_+	834.9	831.0	[kg m^{-3}]
T_-	250.0	250.0	[°C]
X_-	12.0	13.5	[wt.% NaCl]
ρ_-	916.8	919.0	[kg m^{-3}]
Brine	NaCl–H$_2$O	NaCl–CaCl$_2$–H$_2$O	[-]

The subscripts $+$ and $-$ denote the properties for positive and negative initial buoyancy, respectively, in the initial parcel.
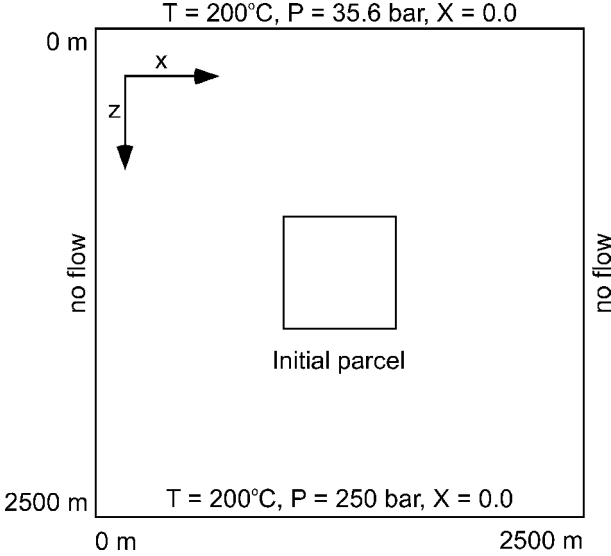
Figure 6. Domain, initial, and boundary conditions for the transient thermohaline convection benchmark as given in Oldenburg and Pruess (1999).

3.3. ENERGY BENCHMARKS

We have also compared our numerical method with results calculated using the well established U.S. Geological Survey's finite difference code HYDROTHERM (Hayba and Ingebritsen, 1994) for pseudo one-dimensional energy transport in pure H_2O at liquid, vapor, two-phase, and supercritical conditions. In all simulations, a hot fluid enters cold fluid-saturated rock from the left and flows down a pressure gradient. The hot fluid displaces and mixes with the cold fluid and heats up the rock. A number of simulations were carried out for heat transport dominated by advection or diffusion, as indicated by the thermal Péclet number Pe_{th} defined as

$$Pe_{th} = \frac{\left(\mathbf{v}_l c_{pl} \rho_l + \mathbf{v}_v c_{pv} \rho_v\right) x_{max}}{\kappa}. \tag{12}$$

Table I lists the rock properties used in the energy benchmarks. Table IV shows the boundary condition and permeability values for advection or diffusion dominated transport. The same spatial resolution of $\Delta x = 2$ m was used in CSP and HYDROTHERM.

Figure 9 shows that there is good agreement between the simulations carried out with CSP and HYDROTHERM at all conditions. The deviation in the energy balance is less than one percent for liquid, vapor, and supercritical conditions and less than two percent at two-phase conditions.

For advection dominated transport, the temperature fronts are always steeper in the CSP simulations, which is due to the second order spatial
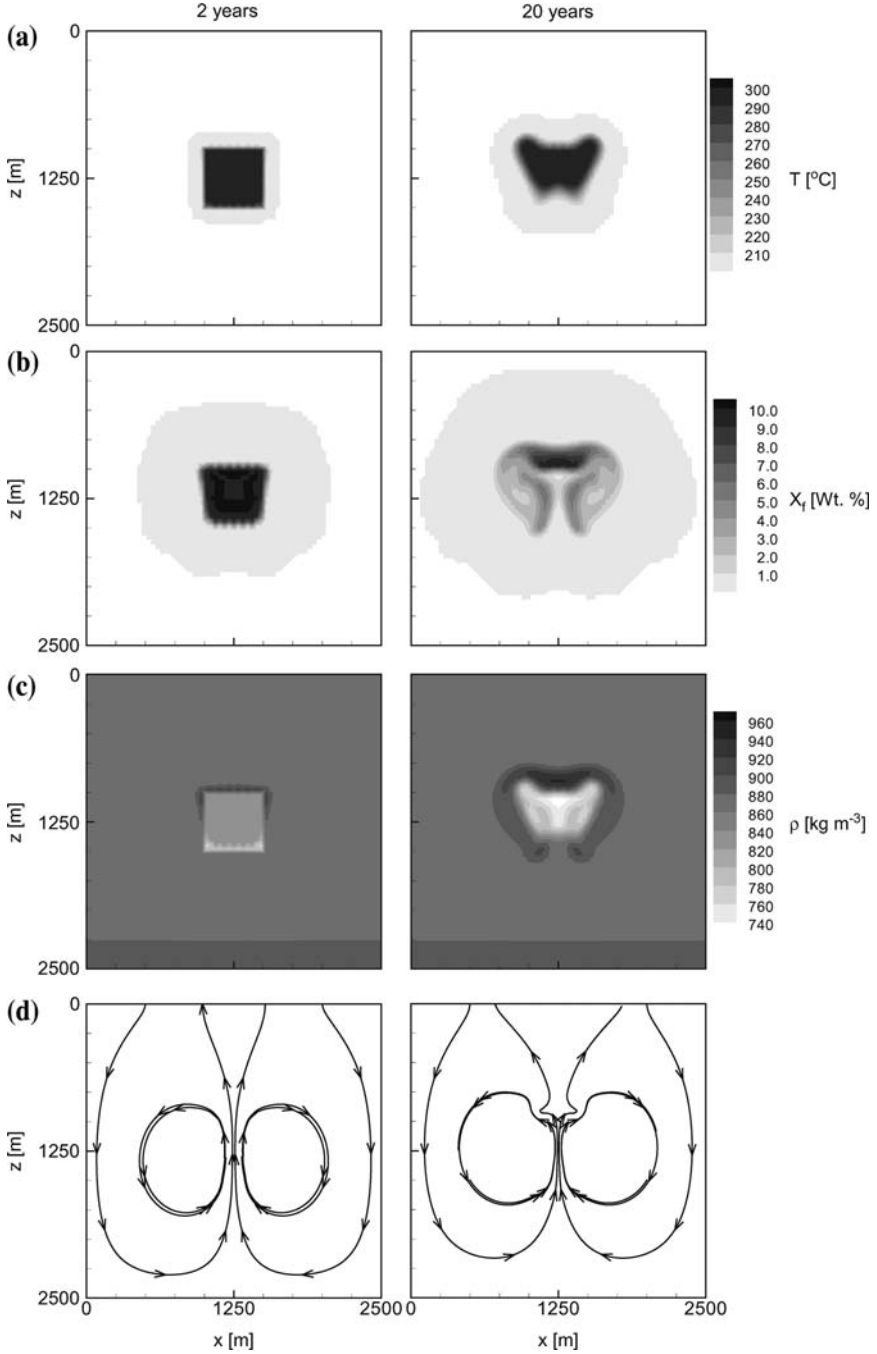
Figure 7. Solution to the positive buoyancy free thermohaline convection problem. From top to bottom: (a) Temperature, (b) brine salinity, (c) fluid density, and (d) streamlines after 2 years (left) and 20 years (right). The streamlines were traced using the velocity field of the respective time-steps.
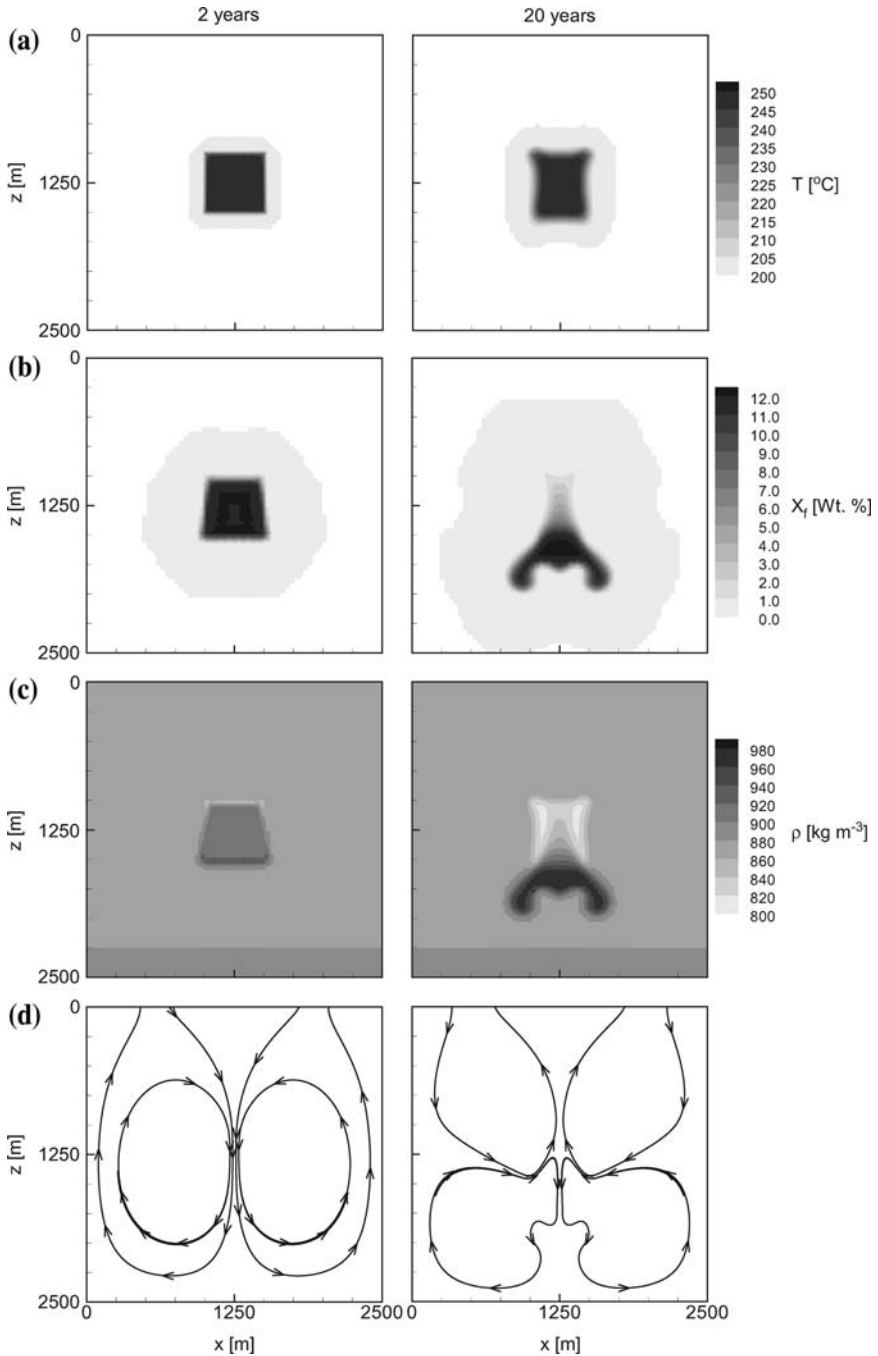
Figure 8. Solution to the negative buoyancy free thermohaline convection problem. From top to bottom: (a) Temperature, (b) brine salinity, (c) fluid density, and (d) streamlines after 2 years (left) and 20 years (right). The streamlines were traced using the velocity field of the respective time-steps.

Table IV. Boundary conditions for energy transport comparisons between CSP and HYDROTHERM for a pure H_2O fluid and advection dominated ($Pe_{th} = 500$) or diffusion dominated ($Pe_{th} = 3$) liquid, vapor, two-phase, and supercritical conditions

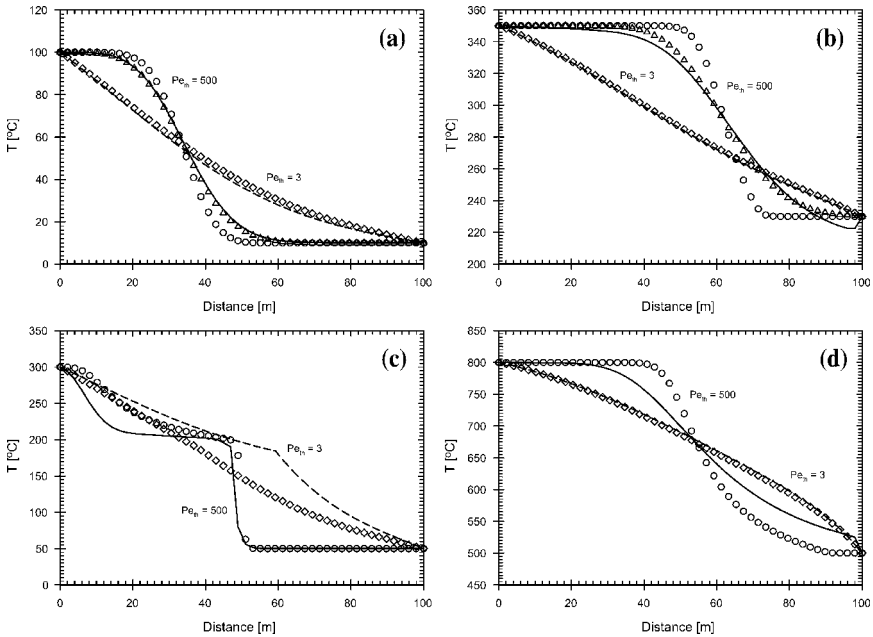| Property	Liquid	Vapor	Two-phase	Supercritical	Unit
$T_{x=0}$	100.0	350.0	300.0	800.0	[°C]
$T_{x=\max}$	10.0	230.0	50.0	500.0	[°C]
$T_{t=0}$	10.0	230.0	50.0	500.0	[°C]
$p_{x=0}$	20.0	20.0	20.0	400.0	[bar]
$p_{x=x_{\max}}$	10.0	10.0	10.0	390.0	[bar]
$k_{Pe_{th}=3}$	5.03×10^{-16}	8.37×10^{-15}	9.91×10^{-16}	1.08×10^{-15}	[m²]
$k_{Pe_{th}=500}$	8.39×10^{-14}	1.40×10^{-12}	1.65×10^{-13}	1.80×10^{-13}	[m²]

Figure 9. Comparison of energy transport in pure H_2O with CSP (open symbols) and HYDROTHERM (lines) at (a) liquid, (b) vapor, (c) two-phase, and (d) super-critical conditions. Simulations were carried out for advection dominated transport at $Pe_{th} = 500$ (circles and bold lines) and diffusion dominated transport at $Pe_{th} = 3$ (diamonds and dashed lines). The triangles at liquid and vapor conditions at $Pe_{th} = 500$ show CSP simulations with a first-order accurate advection scheme. Material properties and initial conditions are listed in Tables I and IV. Profiles were recorded at 0.8 years ($Pe_{th} = 500$) and 30 years ($Pe_{th} = 3$) for liquid conditions, 0.4 years ($Pe_{th} = 500$) and 30 years ($Pe_{th} = 3$) for vapor conditions, 50 days ($Pe_{th} = 500$) and 26 years ($Pe_{th} = 3$) for two-phase conditions, and at 0.8 years ($Pe_{th} = 500$) and 30 years ($Pe_{th} = 3$) for supercritical conditions.

accuracy of our advection scheme. HYDROTHERM only uses a first order accurate spatial resolution. If the spatial resolution in CSP is reduced to first order accuracy, the temperature fronts are also in very good agreement for advection dominated transport (Figure 9a, b). Coumou *et al.* (2004) have recently demonstrated, however, that it is necessary to use higher-order transport schemes for numerical simulations of high-temperature single-phase convection at high Rayleigh Numbers to detect emergent flow patterns. At two-phase conditions and advection-dominated transport, a steep temperature front is also produced by the first-order accurate transport schemes, because in this case the saturation equation is asymptotically identical with the Buckley–Leverett problem (Young, 1993), which causes a self-sharpening of the saturation front (Helmig, 1997).

At vapor conditions and advection dominated transport (Figure 9b), HYDROTHERM computes temperatures that are lower than the initial temperatures close to the outflow boundary, and this is probably not the correct physical solution. Similarly, at supercritical conditions and advection dominated transport (Figure 9d) the temperature profile in the HYDROTHERM simulation depicts a sharp decrease close to the outflow boundary.

At two-phase conditions and advection dominated transport (Figure 9c), a steep temperature drop is associated with the phase boundary between vapor (left of the temperature drop) and liquid (right of the temperature drop). The temperature profile and location of the phase boundary at advection dominated conditions are in good agreement for the two simulations. A small difference in the position of the saturation fronts can be attributed to the error introduced by the decoupling of the governing equations (Dicks, 1993).

For diffusion dominated transport, however, the temperature profiles and locations of the phase boundary differ. We have not been able to reproduce the HYDROTHERM results for diffusion dominated two-phase energy transport with CSP, even if the spatial resolution in CSP was reduced to first order accuracy. We explain the differences in this particular case as a result of the decoupling of the pressure equation from the energy equation in CSP. The computation of the fluid pressure in HYDROTHERM is a result of the fully coupled and iterative solution of the governing equations while CSP computes the diffusion of the fluid pressure directly. The resulting pressure profiles in HYDROTHERM, overall, yield higher pressures on the vapor side than the CSP simulations. If H_2O is a vapor and the pressure increases, its density increases faster than its enthalpy decreases, hence more energy per unit pore volume is transported at higher pressures, and the temperature front moves more rapidly. This effect increases as permeability decreases. We believe that the direct computation of the diffusion of the fluid pressure yields the more

accurate results and that the temperature profiles computed by CSP are more likely to represent the actual physics. For simulations of convective fluid flow, however, the differences between HYDROTHERM and CSP in the temperature profiles at diffusion dominated energy transport are negligible because convection cannot occur if diffusion is the dominant transport process. For the same number of node points, simulations carried out with CSP are generally several times faster than those carried out with HYDROTHERM.

4. Example Application

To illustrate the applicability of our new numerical algorithm, we have modeled the buoyant rise of a hot, saline fluid at 400°C and 10 wt.% NaCl from a depth of 4 km. We use a model-setup that is comparable to the studies of Wilcock (1998), Cherkaoui and Wilcock (1999), and Schoofs *et al.* (1999) (Figure 10, Table V). We apply an open-top boundary condition (Wilcock, 1998; Cherkaoui and Wilcock, 1999), i.e. pressure, temperature, and salinity are held constant at the upper boundary such that fluid can leave or enter through the top boundary. All other boundaries
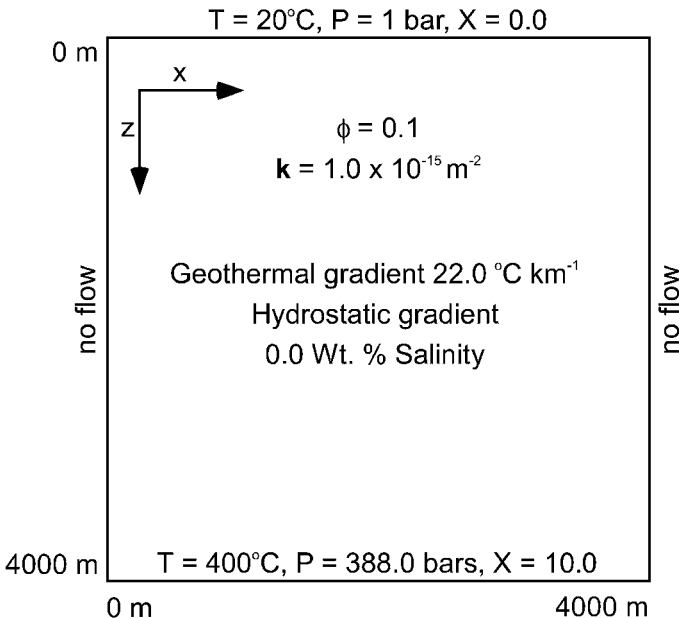

Figure 10. Domain, initial, and boundary conditions for the multiphase thermohaline convection example (see also Table V). An open top boundary is applied by fixing the pressure at 1 bar. This allows fluid to leave or enter through the top boundary (Wilcock, 1998; Cherkaoui and Wilcock, 1999).

are no flow boundaries. Temperature and salinity are also held constant along the bottom boundary at the elevated values of 400°C and 10 wt.% NaCl, respectively. The pressure, however, can vary and is calculated as the current hydrostatic pressure. Initially, the salinity in the porous medium is zero everywhere but along the basal boundary. Away from the basal boundary, the initial geothermal gradient is 22°C km^{-1}. For the applied model-setup, the fluid is a single-phase liquid along the basal boundary. It separates into a high-density, high-salinity brine phase and a low-salinity, low-density vapor phase during its ascent, once the fluid pressure drops below the liquid-vapor surface for the given $T - X$ combination.

4.1. SIMULATION RESULTS

Compared to thermally driven convection in pure H$_2$O, the onset of convection and development of convection cells is delayed. When the convective instability causes hot, saline fluid to move upwards, salt is advected faster than heat. As in the buoyant case in the free thermohaline convection test (Figure 7), this produces a stabilizing high-density lid of relatively cold and saline fluid, which initially opposes the advective rise of the underlying hot and saline fluid. The rising thermal plume and diffusive spreading of the temperature front continuously destabilizes this

Table V. Input parameters for the multiphase thermohaline convection example

Property	Value	Unit
$T_{z=0}$	20.0	[°C]
$X_{z=0}$	0.0	[wt.% NaCl]
$p_{z=0}$	1.0	[bar]
$\rho_{z=0}$	998.2	[kg m^{-3}]
$T_{z=z_{max}}$	400.0	[°C]
$X_{z=z_{max}}$	10.0	[wt.% NaCl]
$p_{z=z_{max}}$	388.0	[bar]
$\rho_{z=z_{max}}$	717.3	[kg m^{-3}]
k	1.0×10^{-15}	[m^2]
ϕ	0.05	[-]
ρ_r	2750	[kg m^{-3}]
c_{pr}	0.88	[kJ kg^{-1} °C^{-1}]
K	2.25	[W m^{-1} °C^{-1}]
a_T	20.0	[m]
a_L	2.0	[m]

a_T and a_L are the transversal and longitudinal dispersivities, respectively.

density stratification. The convection cell begins to form after 200,000 years (Figures 11a and 12a). As the convection cell develops further, salt and energy are quickly advected upwards in a hot, saline, and low-density plume in the center of the model. This central upflow zone develops from a thin basal layer in which the fluid has its maximum temperature and salinity and which persists for the remainder of the simulation. Since salt is transported faster by advection than heat, relatively cold and saline fluid sinks down parallel to the hot, saline upflow zone and the salinity in almost the entire model is larger than ∼5 wt.% NaCl (Figures 11b and 12b). After approximately 233,000 years, the fluid starts to boil in the upflow zone, separating into a high-salinity, high-density brine and a low-salinity, low-density vapor phase. The vapor phase rises quickly, diluting the saline fluid in the shallower parts of the model (Figures 11c and 12c). Within approximately 3,000 years, the flow field reorganizes itself into a narrow upflow zone of hot intermediate salinity fluid (∼ 3−5 wt.% NaCl, and ∼340 − 380°C) feeding a v-shaped boiling zone about 1.5 km below the surface (Figures 11d and 12d). The boiling zone is marked by a discontinuity in the salinity profile. During the reorganization of the flow field, the salinity in the model is continuously reduced until saline fluid exists only in the upflow zone and along the basal boundary. In the boiling zone, part of the low-salinity, low-density vapor continues to rise temporarily precipitating halite. The other part recondenses and the condensate mixes with the high-salinity, high-density brine to form an intermediate density liquid that percolates from the boiling zone downwards parallel to the upflow zone and disperses. Dissolving halite also contributes salt to the intermediate density fluid. Once the reorganization of the flow field is complete, the fluid in the boiling zone cools and the isotherms retract to greater depth. This causes the boiling zone to move upwards, shrink, and vanish after approximately 256,000 years (Figures 11e and 12e). Once the boiling zone has vanished, a steady-state convection cell forms in which hot and intermediate salinity fluid of ∼ 3−5 wt.% NaCl and ∼ 280 − 380°C rises in the center, and cools and sinks down as an intermediate salinity fluid on the flanks (Figures 11f and 12f).

5. Discussion

All benchmark tests show that our results are qualitatively and quantitatively in good agreement with the respective analytical or numerical reference solutions. Also, the example application, which, to the best of our knowledge, for the first time ever included the full complexity of thermohaline convection, demonstrates that our new solution technique yields results that are representative of the geologists qualitative understanding of multiphase thermohaline convection. Field data, for example from porphyry
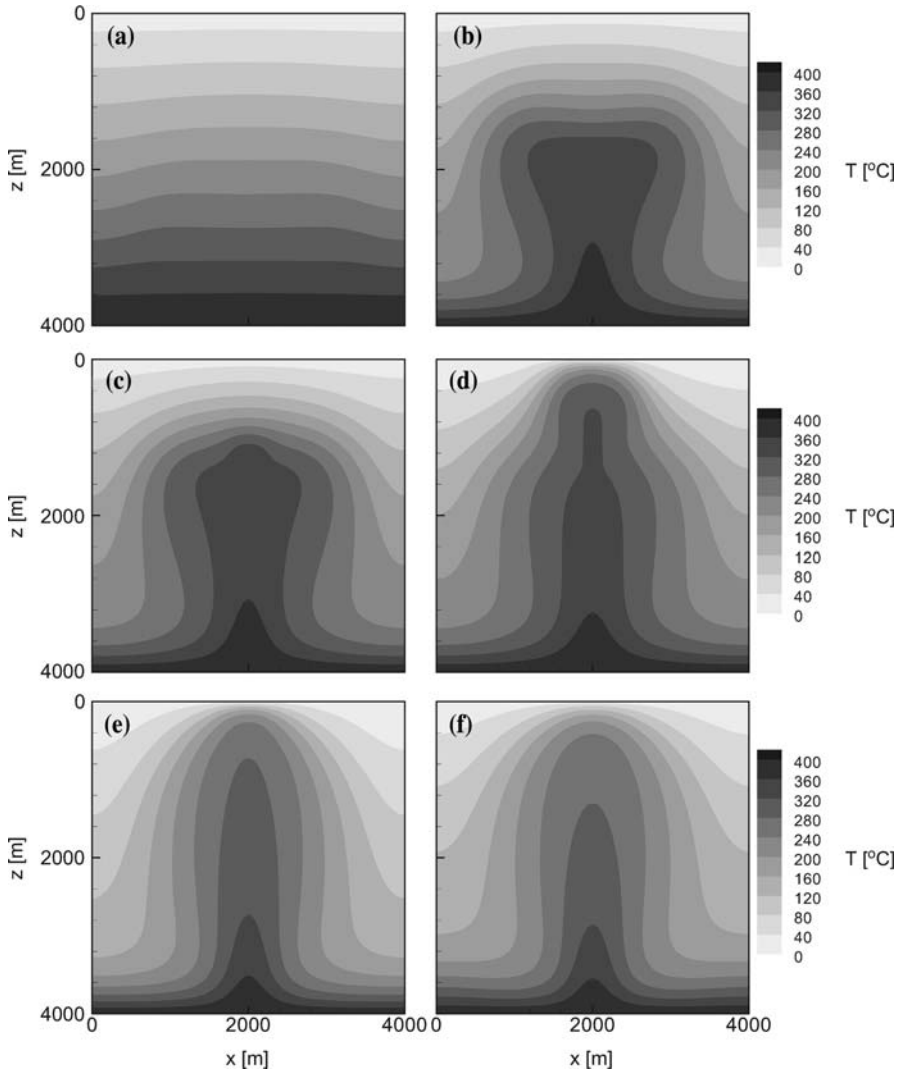
Figure 11. Temperature profiles after (a) 200,000 years, (b) 230,000 years, (c) 232,796 years, (d) 235,239 years, (e) 249,956 years, and (f) 498,709 years.

copper deposits (Henley and McNabb, 1978; Eastoe, 1982), indicates the upward-movement of steam and downward-movement of brines.

This new solution technique now opens the door to realistically and accurately simulate a variety of flow phenomena in geologic processes such as brine convection around cooling magmatic intrusions, flow in oceanic hydrothermal systems, or thermohaline convection of basin brines. These processes could previously only be modeled by making simplifying assumptions such as a pure H_2O fluid, incompressibility, linear dependency
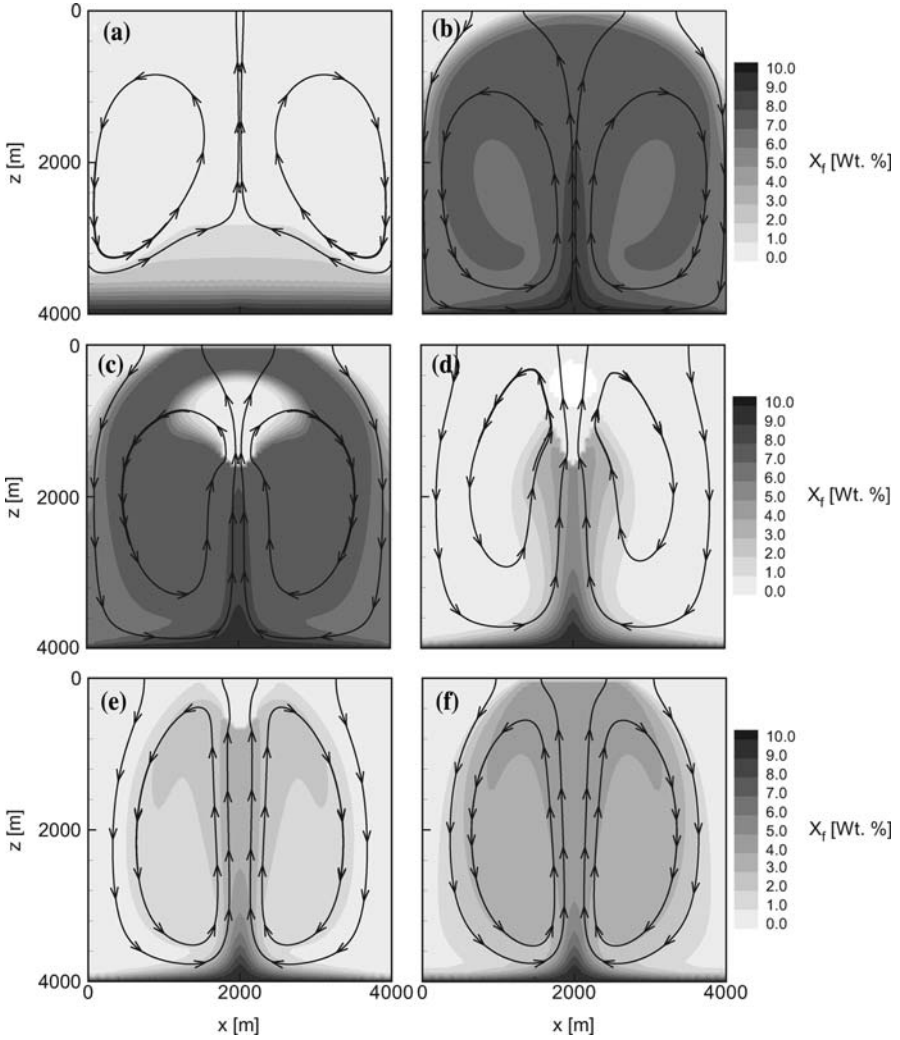
Figure 12. Salinity profiles and streamlines after (a) 200,000 years, (b) 230,000 years, (c) 232,796 years, (d) 235,239 years, (e) 249,956 years, and (f) 498,709 years. Streamlines were traced using the total fluid velocity $\mathbf{v}_f = \mathbf{v}_l + \mathbf{v}_v$ of the respective timesteps. The maximum of the magnitude of the total fluid velocity $|\mathbf{v}_f|$ varies from $\sim 1.0 \times 10^{-9}\,\mathrm{m\,s^{-1}}$ at 200,000 years to $\sim 5.5 \times 10^{-7}\,\mathrm{m\,s^{-1}}$ at 235,239 years.

of density on temperature and salinity, or the absence of phase separation. With the presented work, we have developed a code that can improve our current understanding of the above flow processes.

For future applications it would be desirable if our numerical method could be further benchmarked against field or experimental data, e.g. from geothermal fields, and against other numerical codes that have the

capability of modeling multiphase thermohaline convection with a realistic equation of state of NaCl–H_2O. Little is known about the hydrodynamics of a boiling saline fluid. Only if several codes can be applied to model a suite of thermohaline convection test cases and if these results can be compared to field or experimental data, we will be certain to distinguish numerical artifacts from actual physical process. This will help us to continuously improve the quality of our simulations and will also increase our quantitative understanding of geologic flow phenomena that include the transport of heat and salt. Such benchmarking of numerical methods, for example, has been successfully established with the test cases provided by the Society of Petroleum Engineers to model various aspects of oil–water flow (e.g., Christie and Blunt, 2001).

6. Conclusions

In this paper, we have presented the benchmarking and application of a FEFV framework for numerical simulations of multiphase thermohaline convection. The development of this FEFV technique is discussed in the companion paper (Geiger *et al.*, 2005). A series of test cases, each evaluating a component process of multiphase thermohaline convection, was used for the benchmarking. The algorithm was then applied to model, for the first time ever, the full complexity of convective transport of an initially hot, saline, single-phase liquid phase that is separating into a high-density, high-salinity brine phase and a low-density, low-salinity vapor phase during its ascent.

The simulation framework was implemented into the object-oriented C++ code CSP (Matthäi *et al.*, 2001). Numerical solutions were compared to analytical solutions for the advection-diffusion equation (Ogata and Banks, 1961) and the Buckley–Leverett problem (Buckley and Leverett, 1942; Helmig, 1997), reference solutions for the Elder problem (Elder, 1967) and thermally driven convection at varying Rayleigh numbers (Caltagirone, 1975; Kimura *et al.*, 1986; Steen and Aidun, 1988; Caltagirone and Fabrie, 1989; Cherkaoui and Wilcock, 1999; Schoofs, 1999), a free single-phase thermohaline convection problem (Oldenburg and Pruess, 1999), and energy transport simulations at liquid, vapor, two-phase, and supercritical conditions for pure H_2O, carried out with the U.S. Geological Survey Code HYDROTHERM (Hayba and Ingebritsen, 1994).

The numerical results of the simulations computed with the new solution technique in CSP all are in good agreement with these benchmarks. This implies that our new scheme accurately captures the transient features of multiphase thermohaline convection. This is true also for a full complexity model where a hot, saline and initially single-phase fluid rises and starts

boil. Upon phase separation, the high-density, high-salinity liquid phase is sinking down due to recondensation of vapor as a single-phase intermediate salinity fluid. The low-density, low salinity vapor phase is rising up quickly diluting the fluid above the boiling zone.

With the help of our FEFV framework and its embedded equation of state for NaCl–H_2O, it is now possible to more accurately model thermohaline convection and fluid flow in geologic environments where p-T-X conditions promote boiling and commonly applied simplifications are invalid.

Acknowledgements

References

Ackerer, P., Younes, A. and Mosé, R.: 1999, Modeling variable density flow and solute transport in porous medium: 1. Numerical model and verification, *Transport Porous Media* **35**, 245–373.

Buckley, S. E. and Leverett, M. C.: 1942, Mechanisms of fluid displacement in sands, *TAIME* **146**, 107–116.

Caltagirone, J. P.: 1975, Thermoconvection instabilities in a horizontal porous layer, *J. Fluid Mech.* **72**, 269–287.

Caltagirone, J. P. and Fabrie, P.: 1989, Natural convection in a porous medium at high Rayleigh numbers. Part I - Darcy's model, *Eur. J. Mech. B - Fluids* **8**, 207–227.

Cathles, L. M.: 1977, An analysis of the cooling of intrusives by groundwater convection which includes boiling, *Econ. Geol.* **72**, 804–826.

Cherkaoui, A. S. M. and Wilcock, W. S. D.: 1999, Characteristics of high Rayleigh number two-dimensional convection in an open-top porous layer heated from below, *J. Fluid Mech.* **394**, 241–260.

Christie, M. A. and Blunt, M. J.: 2001, Tenth SPE comparative solution project: A comparison of upscaling techniques. *SPE Paper presented at the SPE Reservoir Simulation Symposium Houston, Texas, U.S.A.*, SPE66599.

Coumou, D., Geiger, S., Driesner, T. and Heinrich, C. A.: 2004, Numerical modelling of MOR hydrothermal systems: The need to use compressible fluids, realistic EOS and high-resolution meshes, *EOS Transactions AGU, Fall Meeting Supplement* **85**, B13A–0210.

Delaney, P. T.: 1982, Rapid intrusion of magma into wet rock: Groundwater flow due to pore pressure increases, *J. Geophys. Res.* **87**, 7739–7756.

Dicks, E. M.: 1983, Higher order Godounov black-oil simulations for compressible flow in porous media, PhD thesis, University of Reading, U.K.

Driesner, T. and Heinrich, C. A.: 2003, Accurate P-T-X-V-H correlations for the system NaCl-H_2O from 0 to 800 °C, 0 to 500 Mpa, and 0 to 1 X_{NaCl}, *Acta Mineralogica–Petrographica Abstract Ser.* **2**, 55–56.

Driesner, T. and Heinrich, C. A.: The system NaCl–H$_2$O. I. Correlation formulae for phase relations in temperature-pressure-composition space from 0 to 1000°C, 0 to 5000 bar, and 0 to 1 X$_{NaCl}$. *Geochimica Cosmochimica Acta*, in revision.

Driesner, T.: The system NaCl–H$_2$O. II. Molar volume, enthalpy, and isobaric heat capacity from 0 to 1000°C, 0 to 5000 bar, and 0 to 1 X$_{NaCl}$. *Geochimica Cosmochimica Acta*, in revision.

Dutrow, B. and Norton D.: 1995, Evolution of fluid pressure and fracture propagation during contact metamorphism, *J. Metamorphic Geol.* **13**, 677–686.

Eastoe, C. J.: 1982, Physics and chemistry of the hydrothermal system at the Panguna porphyry copper deposit, Bougainville, Papua New Guinea, *Econ. Geol.* **77**, 127–153.

Elder, J. W.: 1967, Transient convection in a porous medium, *J. Fluid Mech.* **27**, 609–623.

Geiger, S., Roberts, S., Matthäi, S. K., Zoppou, C. and Burri, A.: 2004, Combining Finite element and finite volume methods for efficient multiphase flow simulations in highly heterogeneous and structurally complex geologic media, *Geofluids* **4**, 284–299.

Geiger, S., Driesner, T., Heinrich, C. A. and Matthäi, S. K.: 2006, Multiphase thermohaline convection in the Earth's crust: I. A new finite element – finite volume solution technique combined with a new equation of state for NaCl–H$_2$O, *Transport Porous Media* **63**, 399–434.

Haar, L., Gallagher, J. S. and Kell, G. S.: 1984, *NBS/NRC Steam Tables*, Hemisphere Publishing Corporation, Washington, DC.

Hayba, D. O. and Ingebritsen, S. E.: 1994, *The Computer Model HYDROTHERM, A Three-Dimensional Finite-Difference Model to Simulate Ground-Water Flow and Heat Transport in the Temperature Range of 0 to 1200°C.* U.S. Geological Survey Water-Resources Investigations Report 94–4045.

Hayba, D. O. and Ingebritsen, S. E.: 1997, Multiphase groundwater flow near cooling plutons, *J. Geophys. Res.* **102**, 12235–12252.

Heinrich, C. A., Günther, D., Audétat, A., Ulrich T. and Frischknecht R.: 1999, Metal fractionation between magmatic brine and vapor, determined by microanalysis of fluid inclusions, *Geology* **27**, 755–758.

Helmig, R.: 1997, *Multi-phase Flow and Transport Processes in the Subsurface*, Springer-Verlag, Berlin.

Henley, R. W. and McNabb A.: 1978, Magmatic vapor plumes and ground-water interaction in porphyry copper emplacement, *Econ. Geol.* **73**, 1–20.

Jupp, T. and Schultz, A.: 2000, A thermodynamic explanation for black smoker temperatures, *Nature* **403**, 880–883.

Kimura, S., Schubert, G. and Straus, J. M.: 1986, Route to chaos in porous-medium thermal convection, *J. Fluid Mech.* **116**, 305–324.

Kolditz, O., Ratke, R., Diersch, H. J. and Zielke, W.: 1998, Coupled groundwater flow and transport: 1. Verification of variable density flow and transport models, *Adv. Water Resour.* **21**, 27–46.

Matthäi, S. K., Geiger, S. and Roberts, S.: 2001, *Complex Systems Platform: CSP3D3.0: User's Guide.* http://e-collection.ethbib.ethz.ch/show?type=bericht&nr=239, Eidgenössische Technische Hochschule Zürich, Switzerland.

Nehlig, P.: 1991, Salinity of oceanic hydrothermal fluids – a fluid inclusion study, *Earth and Planetary Sci. Lett.* **102**, 310–325.

Norton, D. and Knight, J. E.: 1977, Transport phenomena in hydrothermal systems: Cooling plutons, *Amer. J. Sci.* **277**, 937–981.

Ogata, A. and Banks, R. B.: 1961, A solution of the differential equation of longitudinal dispersion in porous media, *U.S. Geological Survey Professional Paper* 411-A.

Oldenburg, C. and Pruess, K.: 1999, Plume separation by transient thermohaline convection in porous media, *Geophys. Res. Lett.* **26**, 2997–3000.

Phillips, O. M.: 1991, *Flow and Reactions in Permeable Rocks*, Cambridge University Press, Cambridge.

Pruess, K.: 1987, *TOUGH User's Guide*. U.S. Nuclear Regulatory Commission, Report NUREG/CR–4645.

Pruess, K.: 1991, *TOUGH2 - A General Purpose Numerical Simulator for Multiphase Fluid and Heat Flow*, Lawrence Berkeley Laboratory Report, LBL–29400.

Roedder, E.: 1971, Fluid inclusion studies on porphyry-type ore deposits at Bingham, Utah, Butte, Montana, and Climax, Colorado, *Econ. Geol.* **66**, 98–120.

Schoofs, S.: 1999, Thermochemical convection in porous media. An application to hydrothermal systems and magmatic intrusions, *Geologica Ultraiectina* **179**.

Schoofs, S., Spera, F. J. and Hansen, U.: 1999, Chaotic thermohaline convection in low-porosity hydrothermal systems, *Earth and Planetary Sci. Lett.* **174**, 213–229.

Simpson, M. J. and Clement, T. P.: 2003, Theoretical analysis of the worthiness of the Henry and Elder problems as benchmarks of density-dependent groundwater flow, *Adv. Water Resour.* **26**, 17–31.

Spivak S, Price, H. S. and Settari, A.: 1977, Solution of the equations for multidimensional, two-phase, immiscible flow by variational methods, *Soc. Petrol. Eng. J.* **17**, 27–41.

Steen, P. H. and Aidun, C. K.: 1988, Time-periodic convection in porous media: transition mechanism, *J. Fluid Mech.* **196**, 263–290.

Strang, G.: 1968, On construction and comparison of difference schemes, *SIAM J. Numer. Anal.* **5**, 506–517.

Sourirajan, S. and Kennedy, G. C.: 1962, The system H_2O-NaCl at elevated temperatures and pressures, *Amer. J. Sci.* **260**, 115–141.

Von Damm, K. L.: 1995, Controls on the chemistry and temporal variability of seafloor hydrothermal fluids, in: S. E. Humphris, R. A. Zierenberg, L. S. Mullineaux, and R. E. Thomson (eds.), *Seafloor Hydrothermal Systems, Geophysical Monograph*, **91**, 222–247.

Wilcock, W. S. D.: 1998, Cellular convection models of mid-ocean ridge hydrothermal circulation and temperatures of black-smoker fluids, *J. Geophys. Res.* **103**, 2585–2596.

Young, R.: 1993, Two-phase geothermal flows with conduction and the connection with Buckley-Leverett theory, *Transport Porous Media* **12**, 261–278.

Zyvoloski, G. A., Robinson, B. A., Dash, Z. V. and Trease, L. L.: 1996, *Users Manual for the FEHMN Application*. Los Alamos National Laboratory, LA–UR–94–3788.